COMMUNICATIONS CHEMISTRY

ARTICLE

DOI: 10.1038/s42004-018-0041-z OPEN

Revealing salt-expedited reduction mechanism for hollow silicon microsphere formation in bi-functional halide melts

Gyujin Song[1], Jaegeon Ryu[1], Jin Chul Kim[1], Jeong Hyeon Lee[1], Sungho Kim[1], Chongmin Wang[2], Sang Kyu Kwak[1] & Soojin Park[1]

The thermochemical reduction of silica to silicon using chemical reductants requires high temperature and has a high activation energy, which depends on the melting temperature of the reductant. The addition of bi-functional molten salts with a low melting temperature may reduce the required energy, and several examples using molten salts have been demonstrated. Here we study the mechanism of reduction of silica in the presence of aluminum metal reductant and aluminum chloride as bi-functional molten salts. An aluminum–aluminum chloride complex plays a key role in the reduction mechanism, reacting with the oxygen of the silica surfaces to lower the heat of reaction and subsequently survives a recycling step in the reaction. This experimentally and theoretically validated reaction mechanism may open a new pathway using bi-functional molten salts. Furthermore, the as-synthesized hollow porous silicon microsphere anodes show structural durability on cycling in both half/full cell tests, attributed to the high volume-accommodating ability.

[1] Department of Energy Engineering, School of Energy and Chemical Engineering, Ulsan National Institute of Science and Technology (UNIST), Ulsan 44919, Republic of Korea. [2] Environmental Molecular Sciences Laboratory, Pacific Northwest National Laboratory, Richland, WA 99352, USA. These authors contributed equally: Gyujin Song, Jaegeon Ryu, Jin Chul Kim. Correspondence and requests for materials should be addressed to S.K.K. (email: skkwak@unist.ac.kr) or to S.P. (email: spark@unist.ac.kr)

Crystallogen compounds have been the backbone of various energy applications[1–4], leading to the developments of further purification methods for its naturally occurring oxide forms. Elimination of oxygen elements from well-defined structure requires a high energy, in principle, which can be viable through gaseous reduction by hydrogen or natural gas[5], solvothermal reduction[6], and thermochemical reduction reaction (TRR)[7–10]. Among them, thermochemical process has been extensively investigated owing to its cost-effectiveness, scalability, precise quantification of precursors based on the stoichiometry, and versatility toward multiple choices of metal oxides[11–13]. The conversion of Si from SiO_2 through thermochemical process provides a general understanding on their mechanism under the given principle of Ellingham diagram, and as-reduced semiconducting Si materials have been particularly utilized as anodes in lithium-ion batteries (LIBs)[13–16].

Typical thermochemical process follows one-to-one exchange of oxygen atoms between metal reductants and SiO_2 initiated by a sufficient thermal energy (carbon for >1400 °C and metals for >420 °C)[17]. As activated carbon or metal reductants undergo the explosive reactions of M (metal or carbon) + SiO_2 (s) → MO_2 + Si (s), easily etchable by-products are generated along with a large amount of exothermic heat. This extensive and accumulated energy of entire system will greatly increase the risk of explosion, and accordingly, appropriate mediation of system energy should be addressed. For this purpose, salt-assisted thermochemical reactions are proposed, where the molten salts absorb the heat of reactions (ΔE) and slow down the overall kinetics[13,18–20]. However, even at this configuration, it is obvious that reactants are supposed to follow the above reaction path and molten salts perform the role of heat scavengers, which do not have any influence on types, spontaneity, and thermal redox pair of reactions.

The role of molten salts recently extended far beyond a kinetic controller and rather effectively participated in the reduction process by providing a reactive medium to the system; Lin et al. introduced a low-temperature molten salt process[21]. It was demonstrated that SiO_2 can be reduced in the presence of metallic aluminum (Al) and aluminum chloride ($AlCl_3$) molten salt medium at relatively low temperature of around 250 °C. Unlike a conventional understanding of the thermochemical process, metal reductants are not directly activated by thermal energy from outside, but assumed to be activated by excessive molten salt streams, indicating that $AlCl_3$ molten salts take part in the reaction. Besides, the proposed driving force of this reaction is an ionization process, which could occur to produce ions and electrons at solvated state with strong reducing power. In addition, Zhou et al. adapted the same experimental set up for the formation of Si hollow microspheres[22], while crucial questions such as exact reaction mechanism of newly proposed reduction systems, a dramatic reduction at low reaction temperature, and influence of $AlCl_3$ in the overall systems are still not unveiled. Although several possibilities were proposed in the previous works, it cannot fully elucidate the whole reaction mechanism of thermochemical process in the molten salt system at such a low temperature.

In this study, we establish the whole reaction pathway for the reduction of SiO_2 with Al metal reductants and in a $AlCl_3$ molten salt medium, named by low-temperature aluminothermic reduction reaction (LTARR), as follows: (i) complex formation between Al and $AlCl_3$, (ii) SiO_2 reduction with adsorbed Al-complex, and (iii) recrystallization of Si seed to produce hollow porous Si sphere (HPSS) demonstrated by density function theory (DFT) calculations and consistent with experimental results. In practical application, carbon-coated HPSS electrodes have a stable battery operation for long electrochemical cycling until 800 cycles without any structural degradation, enabled by plenty of pores and void spaces to accommodate large volume change of Si anodes, confirmed through in situ transmission electron microscopy (TEM) measurements. In particular, the large size of HPSS particles—over 3 μm—significantly increases the electrode density without further calendaring process, and thus high volumetric energy density is attained both in half/full cell demonstrations.

Results

Whole reaction pathway of LTARR. The overall procedure to produce HPSS is illustrated in Fig. 1a. When the mixture, composed of various silica sources, metallic Al, and dry $AlCl_3$, was heated well above the melting point of $AlCl_3$ (~192 °C), the LTARR favorably occurred inside a home-made closed reactor. As the reaction proceeded to form a molten salt, silica was disintegrated into crumbs and reduced gradually into the Si to still separate each other. Afterwards, as-produced Si seeds underwent the recrystallization process, assembling themselves to the hollow and porous structure of Si microsphere. Herein, the reduction mechanism on disintegrated silica crumbs was investigated by the DFT calculation (see Supplementary Figure 1 and Computational modeling and simulation details in Methods). In order for the reduction reaction to occur at such a lower temperature compared to the melting point of metallic Al (~660 °C), Al was predicted to be solvated by the molten salts to form a complex. The reduction mechanism is found as a two-stage reaction undergoing two paths; the formation of Al-centered complex with $AlCl_3$ salts and the reduction of silica surface by adsorbed Al–$AlCl_3$ complex (Fig. 1b). Unlike the previous expectation on the reduction reaction by the activated Al[21,23], the mechanism proposed here is the reduction reaction by activated $AlCl^*$ from the ligand of the Al–$AlCl_3$ complex. In forming the activated $AlCl^*$, two reaction paths with slightly different reaction order are suggested from thermodynamic calculations; path a, in which the ligand $AlCl_3$ is solely separated from the Al–$AlCl_3$ complex and successive two-times transfers of chlorines take place, whereas path b, in which $AlCl_2^*$ is detached from Cl-sharing ligand formed through ligand rearrangement and undergoes the transfer of Cl. Detaching oxygen atoms by $AlCl^*$ from the silica surface resulted in the formation of aluminum oxychloride (AlOCl), the by-product of reduction, and a new Si–Si bond is formed. Successive reduction reactions, which generated many AlOCl molecules, could provide a clustering environment of Si atoms to be a Si seed. As confirmed by experimental works, Si seeds, which are made from successive reduction on SiO_2 crumbs, become recrystallized into spherical shell via localized Ostwald ripening process, and inner crystal seeds dissolve away to reduce the surface energy, resulting the formation of HPSS.

Al dissolution in molten salts. For the initiation of the considered reduction reaction, the probable configurations of adsorbed salts and salt-solvated structures on Al metal surface were theoretically investigated. Since dimers and monomers coexist in the molten $AlCl_3$ (ref. [24]) and three $AlCl_3$ units can completely cover a single Al atom on the Al metal surface, two possible conformations of salts in molten state (i.e., $3AlCl_3$ or $Al_2Cl_6 + AlCl_3$) were placed on the bare Al metal surface, respectively. Here, we denoted the group of three separate $AlCl_3$ molecules as $3AlCl_3$ and the group of $AlCl_3$ dimer and monomer as $Al_2Cl_6 + AlCl_3$. More probable structure among them was determined by comparing the adsorption energies and the change of electronic structure by adsorbed salt molecules (Supplementary Figure 2). As $3AlCl_3$ adsorbed onto the surface, a larger adsorption energy (E_{ad}) was released than when $Al_2Cl_6 + AlCl_3$ were adsorbed. The surface charge of the bare Al metal was about

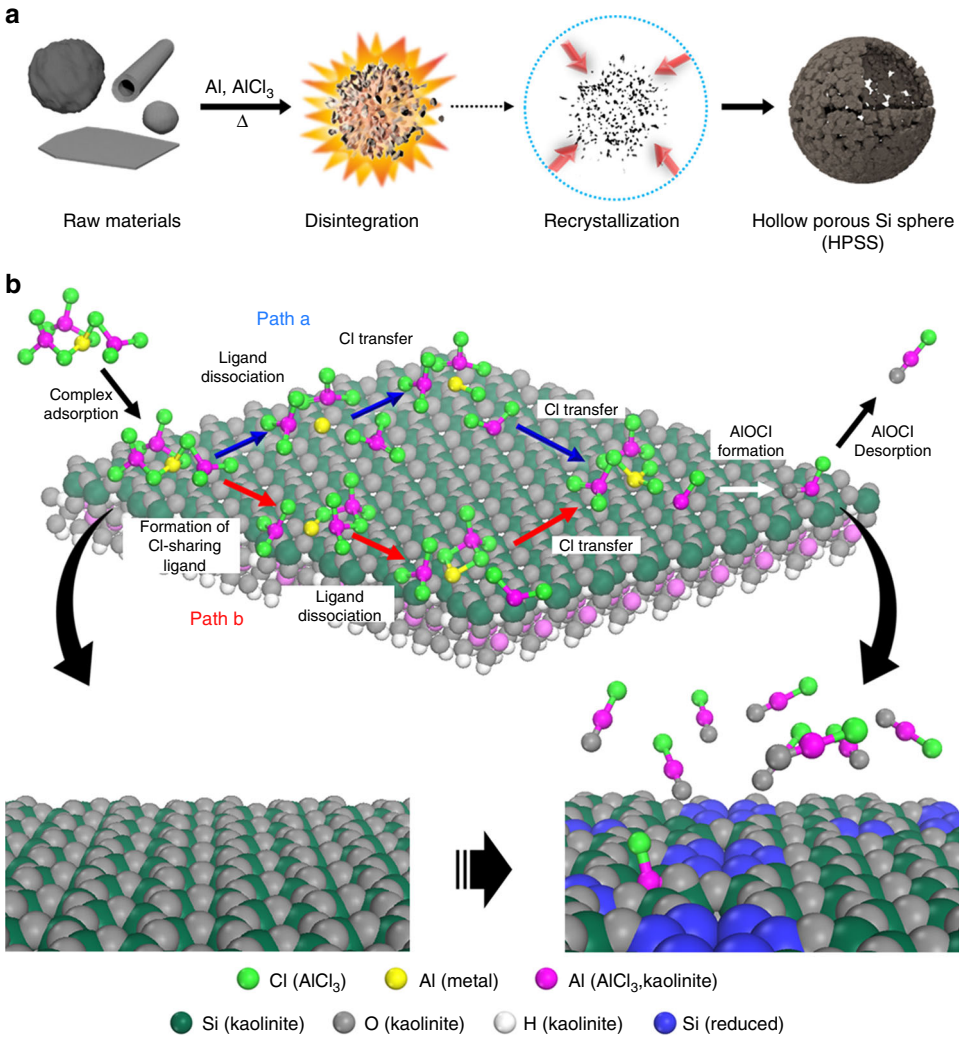

Fig. 1 Schematic illustration of salt-expedited reaction. **a** Chemical reduction process to generate HPSS. Diversely structured SiO_2 raw materials are first disintegrated into smaller Si seeds and then it recrystallizes as time passes. Finally, after leaching out the by-products, HPSS can be obtained. **b** Theoretically tracked reaction mechanism on disintegrated silicate surface to form AlOCl. Path a and path b represent two different pathways to produce activated $AlCl^*$ from the adsorbed Al–$AlCl_3$ complex. Through path a or path b, the Al–$AlCl_3$ complex is dissociated, transferring Cl atoms to form $AlCl^*$. Finally, AlOCl is formed by the as-made $AlCl^*$ reducing SiO_2 in both mechanisms. Atoms of surface and adsorbate are colored differently for the clear view. For kaolinite surface, Al and Si atoms are colored in pink and deep green, and O, H, and clustered Si atoms are colored in light gray, white, and blue, respectively. In the case of the adsorbate, Al and Cl in ligand, and Al center are colored in pink, green, and yellow, respectively

0.085*e* on an average, where overall charge was between 0.078*e* and 0.095*e*. When Al_2Cl_6 molecule was adsorbed on the surface, the partial charges of Al atoms around the adsorbent were slightly changed to 0.029–0.173*e*. However, in case of the adsorption of $3AlCl_3$, the Al charges near the adsorbents showed significant changes to −0.617*e* to 0.269*e*. Note that electrostatic potential (ESP)-mapped electron density surface presents the chemical interaction between Al and $AlCl_3$ (Supplementary Figure 2e), in contrast to no interaction of Al_2Cl_6 with Al (Supplementary Figure 2f). As shown in Supplementary Figure 3a, we estimated that Al dissolution required energy about 1.14 eV, whereas a stable dissolution structure by $Al_2Cl_6 + AlCl_3$ could not be acquired. While an Al atom was detached from the metal surface by $3AlCl_3$, it was coordinated with Al and Cl atoms of two adjacent $AlCl_3$ molecules at distances of 2.6 and 2.4 Å, respectively (Supplementary Figures 3b–d); the Al–$AlCl_3$ complex was formed.

Figure 2 shows an experimental observation of Al dissolution accelerated by the molten salts. Pristine Al metals have a typical spherical structure (1–10 μm) with a smooth surface, while its size should be maintained as small as possible to guarantee the reduction reaction as previously reported (Fig. 2a)[21]. In order to realize the interaction between Al metal and $AlCl_3$ salts, the mixture of two components reacted in the same manner without silica sources. After the reaction, bulging parts in the products were assumed to be Al metals embedded in a solidified salt, and this will be readily converted to an aluminum hydroxide matrix due to extremely sensitive nature of $AlCl_3$ to air and the hydroxyl group, which understandably exists on Al metal surfaces as shown in Fig. 2b, f. Upon its exposure to moisture in air, the composite products were oxygen-contaminated to form a dissolvable $Al(OH)_3$, and subsequent washing process with water removed any other impurities. Furthermore, AlOCl compounds were not formed in the absence of silica precursors, suggesting that AlOCl compounds should be produced with the interaction of both oxygen-included reactants materials and Al–$AlCl_3$ complex. Interestingly, the reacted surface of Al metals, which eliminate $AlCl_3$ and aluminum hydroxide matrix, was caved in or had a porous structure, otherwise it would completely collapse out of shape (Fig. 2c–f). However, it still had a crystalline

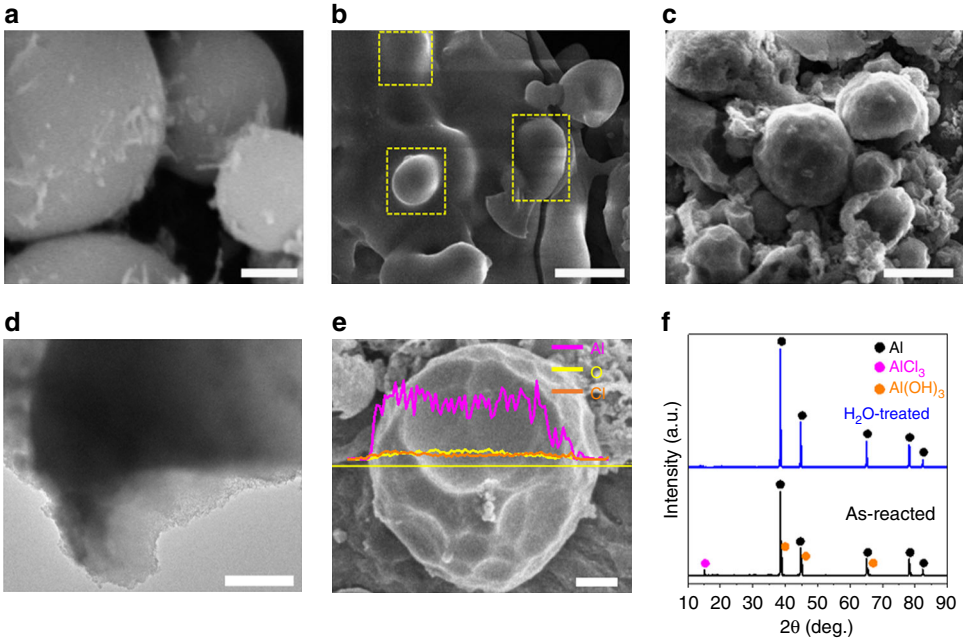

Fig. 2 Al dissolution by molten salts. SEM images of **a** pristine Al and **b** as-reacted sample. Yellow boxes in **b** correspond to $AlCl_3$/$Al(OH)_3$ compounds formed on the Al metal surface. **c** SEM image, **d** TEM image, and **e** magnified SEM image with distribution profile of each atoms (magenta-Al, yellow-O, and orange-Cl) of samples after H_2O treatment. **f** XRD patterns comparison of as-reacted sample and after H_2O treatment. Scale bars, 4 μm (**a**–**c**); 500 nm (**d**); 1 μm (**e**)

property, which implies that excess amounts of salts fully enveloped the Al metals, and at the interface, $AlCl_3$ monomers from molten salts were adsorbed on the Al to promote the formation of Al–$AlCl_3$ complex. This result is consistent with our theoretical calculation results, and the fact that over-stoichiometric amounts of salts are required for the completion of reaction[21]. Dissolution of Al metals in the molten salts creates the reactive species in a form of metal–salt complex and it is expected to initiate the reduction reaction, which counter the previous understanding and hypothesis.

Mechanistic study of AlOCl and Si seed formation. As mentioned earlier, three $AlCl_3$ molecules could entirely surround the fused Al atom dissolved in the molten salt in the form of Al–$AlCl_3$ complex, i.e., $[Al(AlCl_3)_3]$ complex molecule. Central Al was coordinated within 3 Å by the surrounding salt ligands (Supplementary Figure 4a). To elucidate the mechanism of reduction reaction on silica surface, particularly kaolinite surface in this study, we traced the step-by-step pathway to form a new Si-Si bond and the by-product of reduction, AlOCl[20]. The first mechanism considered was the reduction by Al center serving as an activated reductant during the mechanism, as proposed in other works[21,25]. However, the reduction mechanism by Al center (denoted as path 0 in Supplementary Figure 4b) was not preferred because of high activation energy (2.01 eV) caused by the strong interaction of central Al with adjacent $AlCl_3$ molecules. Central Al atom did not fall off the ligand salt molecule, thus a large amount of energy was required for Al to approach the surface close enough to dissociate the Si–O bonds. Instead, it was more preferential that the ligand was separated from the $[Al(AlCl_3)_3]$ complex and adsorbed on the surface. Herein, we suggest another reaction mechanism to yield the activated species from the ligand. The reduction mechanism diverges into two paths, where the order of the reaction is slightly different to form the activated species from the $[Al(AlCl_3)_3]$ complex, i.e., the ligand dissociation (path a) and Al activation (path b) mechanism (Fig. 3). At the first intermediate state of the ligand dissociation mechanism (IM1-a), which had the activation energy (E_a) of 0.64 eV and heat of reaction (ΔE) of −0.41 eV, the ligand $AlCl_3$ itself was detached from the $[Al(AlCl_3)_3]$ complex and solely adsorbed on the SiO_2 surface. On the other hand, at the corresponding state of the Al activation mechanism (IM1-b), the formation of Cl-sharing complex structure by ligand rearrangement required less E_a (0.55 eV) and released more ΔE (−0.72 eV), since the coordination bond between the $AlCl_3$ molecule and central Al needs to be broken once in TS0-a, whereas it remained in TS0-b (Supplementary Figure 4c, d).

Subsequently, in IM2-a, a Cl^* atom of detached $AlCl_3$ was transferred to the Al–$AlCl_3$ complex ($[Al(AlCl_3)_2]$) and the remaining $AlCl_2^*$ interacted with two oxygens on the silica surface, with the E_a of 0.75 eV and ΔE of 0.48 eV. In IM2-b, half of the Cl-sharing ligand was detached and adsorbed on the silica surface in the form of activated $AlCl_2^*$, which strongly reacted with three oxygen atoms on the surface, thus resulting in the E_a of 0.79 eV and ΔE of 0.45 eV, respectively. From IM2 to IM3, the reaction paths of both mechanisms were similar, in that a Cl^* atom was detached once more from $AlCl_2^*$ and the remaining $AlCl^*$ adsorbed to the center of the six-membered ring on the silica surface. At this step, the heat of reaction was observed lower in path a due to the ligand rearrangement of $[Al(AlCl_3)_2Cl]^*$ complex structure to accept the transferred Cl^* (i.e., 0.34 eV for path a and 0.74 eV for path b). As $AlCl^*$ reacted with oxygen in the SiO_2 surface, AlOCl was formed through the dissociations of strong Si–O bonds, following the path a and path b with the highest E_a of 1.44 eV and 1.41 eV along with the ΔE of 1.05 eV and 0.97 eV, respectively. Subsequently, two Si atoms were left to form a new Si–Si bond. Overall, we suggest that Al activation mechanism (path b) provides kinetically and thermodynamically favorable route, although both reaction paths are likely to occur together because of the temperature being as high as 250 °C.

From our observations, ligand $AlCl_3$ could make AlOCl, and Al atom from metallic Al worked as the activated chlorine acceptor at the center of the complex structure. Additionally, we investigated whether the by-product of AlOCl formation (i.e.,

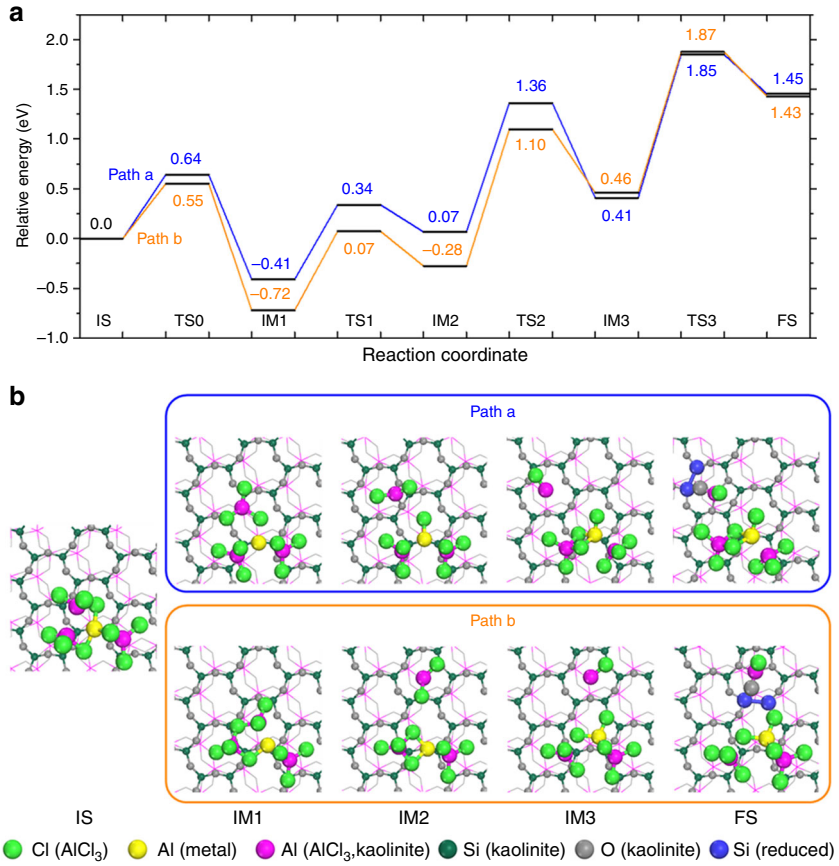

Fig. 3 Reaction mechanism of salt-expedited Si reduction. **a** Reaction coordinate of two reaction mechanisms (i.e., path a and path b). **b** Optimized configurations of the reaction states of each mechanism: IS for initial state of adsorbed Al–$AlCl_3$ complex on the SiO_2 surface, IM1–IM3 for reaction intermediates, and FS for final state, where a Si–Si bond and AlOCl are formed. The numbers in **a** represent the relative energies of each state based on that of the IS. For the clear view, hydrogen atoms in kaolinite are omitted and bottom layers of kaolinite are presented by line model. The others are shown in ball-and-stick model. Color scheme is the same as Fig. 1b

$[Al(AlCl_3)_2Cl_2]^*$ complex structure) could be recycled though a reconstruction procedure. With adjacent $[Al(AlCl_3)_2Cl_2]^*$ complex molecules, mutual exchange of Cl^* atoms resulted in the formation of several $AlCl_3$ molecules and Al-centered new complex, which will act as a new reactant for further reduction reactions (Supplementary Figure 5). Through the complex reconstruction, three $[Al(AlCl_3)_2Cl_2]^*$ complexes are transformed into Al_2Cl_6 and $AlCl_3$ molecules, as well as a new $[Al(AlCl_3)_2]$ complex (i.e., $3[Al(AlCl_3)_2Cl_2]^* \rightarrow [Al(AlCl_3)_2] + 6AlCl_3$). In summary, the reaction formula considered with three $[Al(AlCl_3)_3]$ complexes in this study can be expressed as,

$$3Al + 9AlCl_3 \rightarrow 3Al(AlCl_3)_3 \quad (1)$$

$$3Al(AlCl_3)_3 + 3/2\,SiO_2 \rightarrow 3\left[Al(AlCl_3)_2Cl_2\right]^* + 3AlOCl + 3/2\,Si \quad (2)$$

followed by the reconstruction of the reaction by-product $[Al(AlCl_3)_2Cl_2]^*$.

$$2\left[Al(AlCl_3)_2Cl_2\right]^* \rightarrow \left[Al(AlCl_3)_2Cl\right]^* + Al_2Cl_6 + AlCl_3 \quad (3)$$

$$\left[Al(AlCl_3)_2Cl_2\right]^* + \left[Al(AlCl_3)_2Cl\right]^* \rightarrow Al(AlCl_3)_2 + Al_2Cl_6 + AlCl_3 \quad (4)$$

By summing up all these reaction formulae, the overall reaction is written as,

$$3Al + 9AlCl_3 + 3/2SiO_2 \rightarrow 3AlOCl + Al + 8AlCl_3 + 3/2Si \quad (5)$$

which is consistent with previous experimental suggestion[21].

$$4Al + 2AlCl_3 + 3SiO_2 \rightarrow 6AlOCl + 3Si \quad (6)$$

Evolution of HPSS. Through step-by-step validations on overall reaction mechanism of low-temperature reduction process, we revealed that molten salts served as a promoter for Al metal dissolution and the thus-stabilized complex structure broke the very strong Si–O bond, leading to the formation of Si–Si bond. The as-produced Si seed had a relatively free motion in the salts stream at a temperature above its melting point, while it was self-assembled in a way of reducing the surface energy of particles upon cooling off (i.e., spherical structure). However, concurrently generated AlOCl and small Si crystal seeds will be necessarily embedded together with remaining $AlCl_3$ salts in a Si sphere. As a result, these residues dissolved away and led to a construction of hollow and porous structure, regardless of various silica sources (Supplementary Figures 6 and 7).

Figure 4a–d shows stepwise SEM images of HPSS prepared from halloysite clay minerals, which was chosen for its available purity and cost, as mentioned previously[21,22]. After complete reduction, densely packed spheres are embedded in a stream of

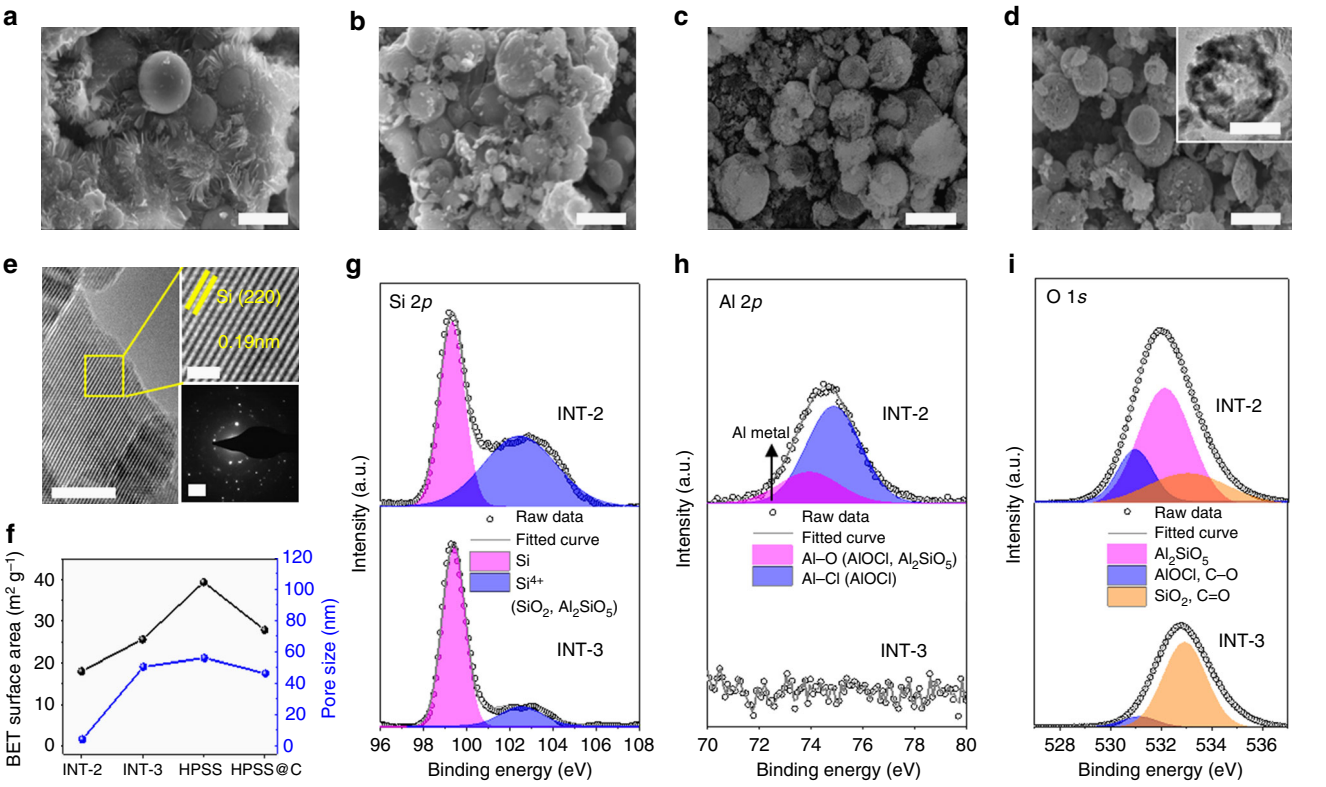

Fig. 4 Structural evolution of HPSS. SEM images of samples at various stages; **a** INT-1, **b** INT-2, **c** INT-3, and **d** after HF treatment (denoted as HPSS, an inset corresponding to TEM image of HPSS). **e** Magnified TEM image of HPSS (an inset corresponding to High-resolution TEM image and selected area electron diffraction pattern). **f** BET surface area values and pore volumes of after-dissolving water (INT-2), after HCl treatment (INT-3), HPSS, and HPSS@C. **g**–**i** XPS spectra of Si 2*p*, Al 2*p*, and O1s of INT-2 and INT-3 samples. Scale bars, 4 μm (**a**–**d**); 5 nm, 2 nm, and 2 1/nm (**e**)

excessive solidified molten salts. The subsequent water and leaching steps remove any other impurities and consequently lead to a pore generation both inside the shells and at the core, as shown in the inset of Fig. 4d. The typical polycrystalline nature of HPSS was observed in high-resolution transmission electron microscopy (HR-TEM) images with lattice fringes of 0.19 nm spacing, corresponding to (220) plane and selected area electron diffraction (SAED) pattern (Fig. 4e). The X-ray diffraction (XRD) pattern confirmed sequential phase transitions into the final Si and the formation of crucial by-products of AlOCl, which could further validate our proposed mechanism (Supplementary Figure 8). Based on X-ray photoemission spectroscopy (XPS) results, Al existed primarily as AlOCl and Al metals, while HCl completely removed these compounds without any traces, confirming that this LTARR method provides high-purity Si products, also corroborated by Si and O spectra (Fig. 4g–i and Supplementary Figure 9).

Nitrogen sorption measurements were conducted to quantify the surface area and porosity of HPSS. During the post treatments, its value gradually increased, as etching out the residual components (Al, AlOCl, amorphous Al_2O_3, and SiO_2) and the surface area of HPSS is 39.4 $m^2\ g^{-1}$ with pore size of ~56 nm (Fig. 4f, see detailed results in Supplementary Figure 10). In addition, various factors were investigated for further demonstration of this mechanism, such as reaction time, temperature, and existence of Al metal (Supplementary Figures 11–13). Apart from this variation, there are additional factors governing this reduction process. Size of metals, stoichiometry of reactants, and reaction environments are cases in point, while these issues have already been discussed in the previous report[21,22] and are out of scope for this study. It should be noted that our mechanism could be directly applied to different metal centers for the complex structure as well as chlorine acceptor as discussed earlier, thus successfully producing a hollow and porous structured Si.

Electrochemical study. HPSS has comparable features of a porous shell and a core void available in a microparticle, which offers a viable choice for Si anodes, according to the recent novel designs[3,4,15,26–28]. For validation on capability of HPSS to accommodate volume changes, in situ TEM analysis was carried out to monitor a dynamic behavior upon lithiation and delthiation with a nanobattery setup (Supplementary Figure 14). Before measurement, carbon-coating layers were introduced to improve the electric conductivity of HPSS particle (denoted as HPSS@C, Supplementary Figure 15). Under a negative bias (−3 V), Li ion diffuses gradually to the HPSS@C particle in Fig. 5a to proceed the lithiation, and at the end of lithiation for 50 min, a change in the outer diameter of the HPSS@C was negligible due to an inward void filling, even at the crystalline $Li_{15}Si_4$ phase (Fig. 5b, d, and Supplementary Movie 1). During delithiation under a positive bias of 3 V for 22 min, amorphous Si was present, corresponding to the SAED pattern, and recovered to the original structure (Fig. 5c, e, and Supplementary Movie 2). The magnified TEM images of pristine state in Fig. 5f and fully lithiated state of HPSS clearly showed shell thickening and pore fillings, as shown in Fig. 5g. The shell expanded 22%, and the porous shell became dense with a high contrast, filling out both mesopores and macropores. It is notable that the filled pores were recovered after delthiation process, while the shells remained a little swelled to 17% with a great structural integrity, in Fig. 5h. Inner and outer diameters were estimated to calculate the volume variation during lithiation/delithiation (Fig. 5i). Surprisingly, the expansion of the whole particle featured less than 10% and it recovered to only 4%

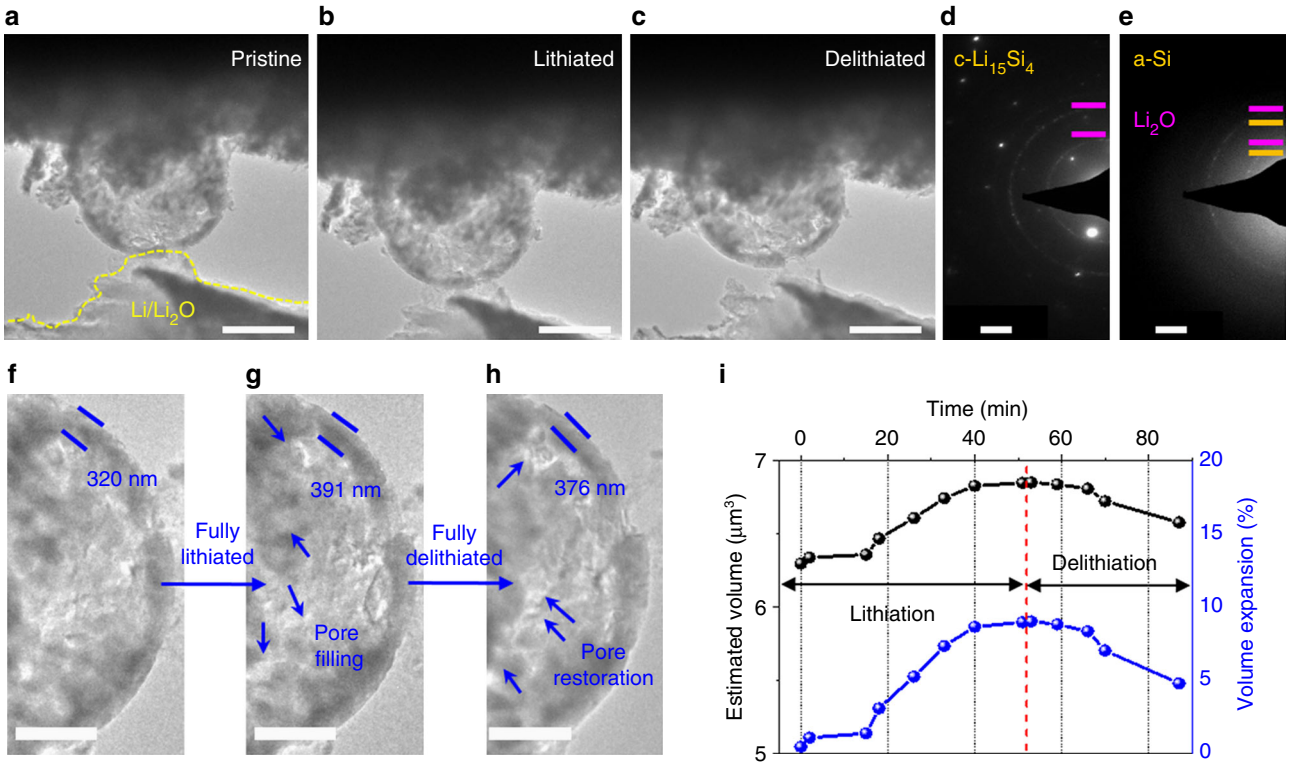

Fig. 5 In situ electrochemical observation of a single HPSS-based particle. **a**–**c** Time-resolved TEM images of single HPSS@C particle during lithiation/delithiation with corresponding selected area electron diffraction (SAED) patterns of **d** fully lithiated and **e** delithiated samples under a potential of −3 V/3 V, respectively. Magnified TEM images of **f** pristine, **g** fully lithiated, and **h** delithiated HPSS@C particle, which illustrate thickened shell (22% expansion after lithaition) and pore filling/restoration showing no structural collapse. **i** Estimated volume and expansion ratio of HPSS@C particle during lithiation/delthiation. Scale bars, 1 μm (**a**–**c**); 2 1/nm (**d**, **e**); 500 nm (**f**–**h**)

swelled state with respect to the pristine. Although the swelling results for non-coated HPSS from in situ analysis had similar values, it required a higher bias to proceed to lithiation, which indicated that carbon layers will facilitate the diffusion of Li ions into the particles, and further electrochemical properties were measured by using the HPSS electrodes (Supplementary Figure 16 and Supplementary Movies 3, 4).

The beneficial effects of HPSS structure on volume accommodation were further demonstrated by galvanostatic charge/discharge tests in both half cell and full cell configuration. The differential capacity curves were consistent with the behavior of typical crystalline Si anodes (Supplementary Figure 17)[29]. Figure 6a shows rate-dependent voltage profiles in a potential window of 0.005–1.5 V and 0.01–1.2 V for initial cycle and subsequent cycles, respectively. The HPSS@C electrode had an initial Coulombic efficiency of 91%, with discharge capacity of 3494 mAh g^{-1}. The irreversible capacity loss is originated from the formation of the solid electrolyte interphase (SEI) and reaction with native oxides[30]. The sufficient channels for electrolyte infiltration and microsphere structure of HPSS enable the electrode to be activated quickly and have such a high initial Coulombic efficiency. Despite bulky structure of HPSS, its electrode afforded a fast charging ability up to 5*C* rate (1*C* = 3.5 A g^{-1}) with a reversible capacity of 1100 mAh g^{-1}, which is still three times higher than that of graphite anode (Supplementary Figure 18). Cycling stability of HPSS@C electrode was monitored for prolonged cycles. HPSS@C electrode delivered reversible capacity of 832 mAh g^{-1} after 800 cycles at 1*C* rate with an average Coulombic efficiency of 99.5%. This extended cycle life of the HPSS@C electrode can be ascribed to effective inward breathing during lithiation and pore restoration during delithiation (Fig. 6b and Supplementary Figure 19). Sluggish diffusion of Li ions through microparticles can be simply redeemed by conductive carbon layers, compared with non-coated HPSS (Supplementary Figure 20). By extension, the full cell evaluation was conducted with commercial $LiCoO_2$ (LCO) cathode in the potential window of 2.5–4.2 V. The cycling tests showed a stable capacity retention over 100 cycles, with an end capacity of 2.39 mAh cm^{-2} at 0.2*C* rate (Fig. 6c and Supplementary Figures 21 and 22). Since stable cycling and Li ion diffusion kinetics have a close relation to structural stability and electrode swelling, post characterizations were also carried out. Figure 6d shows a summary chart for electrode thickness change. It should be noted that electrodes expanded 56.4% after 100 cycles without any pulverization or delamination of active materials (Fig. 6e and Supplementary Figure 23) and retained original structures with enough void spaces, which accords with improved electrochemical performances. Along with the structural stability and cyclic performance of HPSS@C in Supplementary Figures 24 and 25, Nyquist plots display low-charge transfer resistance after 50th cycle due to fast electrode activation and shortened Li-ion diffusion path, compared with the results of HPSS that has exposed fresh Si surface to electrolyte, triggering thick or irregular formation of SEI layer on the surface.

Discussion

In this study, we have demonstrated the step-by-step mechanism of LTARR on the silicate surface in the presence of molten $AlCl_3$ salts and electrochemical performance of as-prepared HPSS. By the DFT calculation as well as experimental validation, we showed that adsorption of molten $AlCl_3$ molecules on the Al surface emits a large amount of heat, promoting the detachment

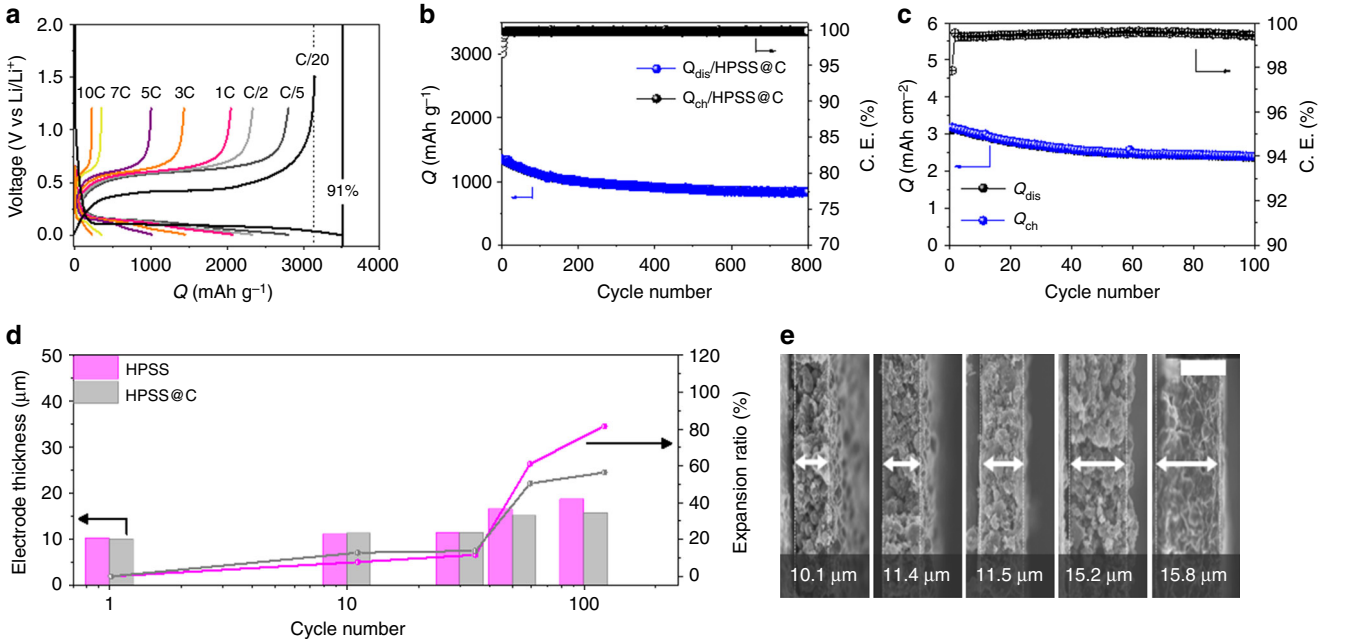

Fig. 6 Electrochemical performance of HPSS-based electrode. **a** Galvanostatic charge–discharge profiles of HPSS@C electrode at different rates. **b** Cycling stability of HPSS@C electrode at 1C rate (3.5 A g^{-1}) for 800 cycles. **c** Cycling performance of full cell employing HPSS@C anode and $LiCoO_2$ cathode for 100 cycles at 0.2C rate (0.62 mA cm^{-2}). **d** Ex situ electrode analysis for thickness change. **e** Cross-sectional SEM images of HPSS@C electrodes of pristine (10.1 μm), 10th (11.4 μm), 30th (11.5 μm), 50th (15.2 μm), and 100th cycle (15.8 μm). Scale bar, 10 μm (**e**)

of Al in the form of Al–$AlCl_3$ complex. Remarkably, dissimilar to expectations of previous research on the reduction by activated Al^* atom forming Al_2O_3 in molten $AlCl_3$, the activated Al^* does not favorably adsorb on the silica surface compared to $AlCl_3$, since a considerable amount of activation energy and heat of reaction are accompanied when detaching oxygen atoms[23]. In this regard, LTARR mechanism can be considered as a ligand-promoted reduction, where the activated $AlCl^*$ produced from the ligand reacted with oxygen atom of the silica surface. Due to the dominant role of the salt molecule in this reduction, the mechanism we have suggested may show the universality of the mechanism of reduction to metals, which can form complex structures with metal halide molecules. In addition, through the reconstruction of $[Al(AlCl_3)_2Cl_2]^*$ molecules and the by-products of AlOCl formation, some fraction of active sites for succeeding reduction are preserved even after a series of reaction.

In terms of electrochemical performance, the as-synthesized HPSS via LTARR through salt-expedited mechanism shows prolonged cycles owing to the pores on the surface and inside voids, which have the role of space-enhancing structure to moderately accept lithium ion during lithiation to maintain the morphology without any breakdown. Further introduction of a carbon-coating layer can improve the lower intrinsic electronic conductivity of Si microparticles.

We expect that the present proposed mechanism could be widely applied to other metals or metal salts system with SiO_2-containing compounds.

Methods

Materials. Halloysite, montmorillonite, kaolinite, nanoclay, nanosized silica (10–20 nm), anhydrous aluminum chloride ($AlCl_3$), and hydrofluoric acid (HF, 49%) were obtained from Sigma-Aldrich. Microsized silica (1 μm), aluminum metal, and hydrochloric acid (HCl, 35–37%) were purchased from Alfa Aesar, Angang, and SAMCHUN, respectively. All chemicals were used without any purification.

Computational modeling and simulation details. We investigated the molten $AlCl_3$ salt-expedited Si-reduction mechanism over silicate surface using Dmol[3] program[31,32]. The reduction mechanism was predicted to be a two-step reaction; the formation of metal complex, which is clustered $AlCl_3$ around atomic Al detached from metallic Al surface, and the reduction of silicate surface by the adsorbed complex. The most stable (111) surface of Al was used when the metal complex was investigated for the calculation. The silicate surface was a monolayer kaolinite, which is the dehydrated form of halloysite, because the reduction reaction occurs with the decomposed crumbs from the halloysite as shown in the experimental procedure. Even though kaolinite has a layered silicate structure, consisting of the corner-sharing SiO_4 sheet linked to the edge-sharing AlO_6 sheet, only reactions on SiO_4 sheet, i.e., kaolinite $(00\bar{1})$ surface, were taken into consideration for mechanism calculation in order to readily observe the formation of a new Si–Si bond. For the DFT calculation, we employed the Perdew–Burke–Ernzerhof exchange-correlation functional[33] and DNP 4.4 basis set with the all-electron relativistic core treatment. The convergence criteria for energy, force, and displacement were set to 1×10^{-5} Ha, 0.002 Ha $Å^{-1}$, and 0.005 Å, respectively. To include the dispersion correction of the van der Waals effect, the Tkatchenko–Scheffler scheme was used[34]. The Brillouin zone was sampled by a Monkhorst–Pack as a single *k*-point (Γ-point) for all model systems. To calculate transition states in the mechanism of Si-reduction, we employed complete single linear synchronous transit (LST) and quadratic synchronous transit (QST) methods[35,36], and the convergence criteria of the root mean square (RMS) force was set as 0.003 Ha $Å^{-1}$. In terms of model systems, we constructed two slab models for trilayer Al (111) and monolayer kaolinite $(00\bar{1})$, respectively (Supplementary Figure 1). Al metal slab model was constructed with the 3×3 supercell of (111) surface and three atomic layers and for the kaolinite slab, the 2×3 supercell of kaolinite $(00\bar{1})$ was used. Note that there were marginal differences in adsorption and reaction energy values (Supplementary Table 1) when the monolayer kaolinite was extended to bilayer and it implies that monolayer is reasonable to trace the reaction mechanism.

HPSS and HPSS@C synthesis. In the Argon (Ar)-filled glove-box, 1.0 g of Halloysite was mixed with 0.8 g of Al and 8.0 g $AlCl_3$ in custom-made stainless steel (SS) reactor with completely sealed. This reactor was transferred to the furnace and then heated at 250 °C for 10 h under Ar atmosphere continuously. After cooling down, the reactor was brought out and as-synthesized product ($Si/SiO_2/AlOCl/AlCl_3$, (INT-1)) was rinsed with deionized water (DI water) for several times, followed by filtrating it with ethanol and DI water and drying at 80 °C overnight ($Si/SiO_2/AlOCl$, (INT-2)). Then, $Si/SiO_2/AlOCl$ sample was leached with 1.0 M HCl for 1 h at 35 °C to remove the AlOCl, followed by same filtration and dry step (Si/SiO_2, (INT-3)). Finally, 5% HF treatment completely eliminate residual SiO_2 with same filtration and dry steps (HPSS). All silicon products using other silica precursors was synthesized by same procedure. Finally, for HPSS@C, HPSS was heated at 900 °C for 1 min in acetylene gas (C_2H_2, 99.9%) at a flow rate of 500 cc min^{-1}.

Materials characterization. The morphological analysis and elemental mapping were carried out by the field-emission scanning electron microscopy (FE-SEM,

Nova 230, FEI) and scanning transmission electron microscopy (STEM, Titan 80-300/FEI) with EDX detector operated at 300 kV. XRD pattern was acquired by using Bruker D8-advance, which were conducted at 3 kW using Cu Kα radiation in the θ range from 20° to 80°. Raman spectra were obtained by a confocal Raman (alpha 300R, WITec) with 532 nm of wavelength laser. Auto Physisorption Analyzer (ASAP2020 Analysis) was used for BET and BJH analysis to investigate the surface area and pore size. For checking carbon weight portion after carbon coating process, thermogravimetric analysis (TGA, Q500) was used with 10 °C min^{-1} ramping rate under oxygen gas (O_2) flow. The XPS (ThermoFisher, K-alpha) analysis were carried out to obtain quantitative/qualitative information on surface oxidation state of samples.

In situ TEM observation. The solid state nanobattery was constructed to observe the electrochemical reaction in the real time as illustrated in Fig. 5a. The samples were loaded on Al wire as the working electrode, which occupied one side of nanofactory STM holder. Li metal was scratched out by the tungsten (W) tip mounted on the other side of the holder as the counter electrode. This process was carried out in Ar-filled glove-box, then, the holder was transferred to the TEM. Li metal was shortly exposed to the air (<2 s) while lithium oxide (Li_2O) was formed to be a solid electrolyte in this system. The electrochemical reaction, lithiation/dethiation was driven by external bias applied to the nanobattery.

Electrochemical characterization. A slurry consisting of active materials, Super-P, and poly (acrylic acid) (PAA)/carboxymethyl cellulose (CMC) (1:1 weight ratio) in a weight ratio of 80:10:10 were blade-coated on Cu foil with active loading level of 1.0–1.5 mg cm^{-2}. 2032-type coin cells (Welcos) were assembled in an Ar-filled glove box using Li metal as the counter/reference electrode, a Celgard 2400 membrane (polypropylene) as the separator, and 1.3 M $LiPF_6$ in a mixture of ethylene carbonate (EC)/diethyl carbonate (DEC) (3:7 v/v) including 10 wt% fluoroethylene carbonate as the electrolyte, and 1 M $LiPF_6$ as the lithium salt under Ar atmosphere. The electrochemical performance was evaluated by galvanostatic measurement using a battery cycler (Wonatech, WBCS-3000) in the operating voltage of 0.005–1.5 V (1st cycle) and 0.01–1.2 V for further cycles at room temperature. In full-cell test, the $LiCoO_2$ (LCO) was adopted as cathode materials with a N/P ratio of ~1.1. The cathode was fabricated with active materials, Super-P, and polyvinylidene fluoride binder (PVdF) in a weight ratio of 95:2.5:2.5. The mass loading level of the cathode was ~19 mg cm^{-2}. The full cells were performed in the operating voltage of 2.5–4.2 V.

Data availability. The authors declare that the data support the findings of this study are available from the corresponding authors on reasonable request.

Received: 16 March 2018 Accepted: 6 July 2018
Published online: 06 August 2018

References

1. Pietsch, P. et al. Quantifying microstructural dynamics and electrochemical activity of graphite and silicon-graphite lithium ion battery anodes. *Nat. Commun.* **7**, 12909 (2016).
2. Billaud, J., Bouville, F., Magrini, T., Villevieille, C. & Studart, A. R. Magnetically aligned graphite electrodes for high-rate performance Li-ion batteries. *Nat. Energy* **1**, 16097 (2016).
3. Ko, M. et al. Scalable synthesis of silicon-nanolayer-embedded graphite for high-energy lithium-ion batteries. *Nat. Energy* **1**, 16113 (2016).
4. Liu, N. et al. A pomegranate-inspired nanoscale design for large-volume-change lithium battery anodes. *Nat. Nanotechnol.* **9**, 187–192 (2014).
5. Choi, S. et al. Generalized redox-responsive assembly of carbon-sheathed metallic and semiconducting nanowire heterostructures. *Nano Lett.* **16**, 1179–1185 (2016).
6. Liang, J. W., Li, X. N., Zhu, Y. C., Guo, C. & Qian, Y. T. Hydrothermal synthesis of nano-silicon from a silica sol and its use in lithium ion batteries. *Nano Res.* **8**, 1497–1504 (2015).
7. Bao, Z. H. et al. Chemical reduction of three-dimensional silica micro-assemblies into microporous silicon replicas. *Nature* **446**, 172–175 (2007).
8. Choi, S., Kim, J., Choi, N.-S., Kim, M. G. & Park, S. Cost-effective scalable synthesis of mesoporous germanium particles via a redox-transmetalation reaction for high-performance energy storage devices. *ACS Nano* **9**, 2203–2212 (2015).
9. Lee, K. J., Choi, S., Park, S. & Moon, H. R. General recyclable redox-metallothermic reaction route to hierarchically porous carbon/metal composites. *Chem. Mater.* **28**, 4403–4408 (2016).
10. Choi, S. et al. Mesoporous germanium anode materials for lithium-ion battery with exceptional cycling stability in wide temperature range. *Small* **13**, 1603045 (2017).
11. Choi, S. et al. Revisit of metallothermic reduction for macroporous Si: compromise between capacity and volume expansion for practical Li-ion battery. *Nano Energy* **12**, 161–168 (2015).
12. Ryu, J. et al. All-in-one synthesis of mesoporous silicon nanosheets from natural clay and their applicability to hydrogen evolution. *NPG Asia Mater.* **8**, e248 (2016).
13. Favors, Z. et al. Scalable synthesis of nano-silicon from beach sand for long cycle life Li-ion batteries. *Sci. Rep.* **4**, 5623 (2014).
14. Wang, W. et al. Monodisperse porous silicon spheres as anode materials for lithium ion batteries. *Sci. Rep.* **5**, 8781 (2015).
15. Xiao, Q. F. et al. Inward lithium-ion breathing of hierarchically porous silicon anodes. *Nat. Commun.* **6**, 8844 (2015).
16. Jung, D. S., Ryou, M. H., Sung, Y. H., Park, S. B. & Choi, J. W. Recycling rice husks for high-capacity lithium battery anodes. *Proc. Natl Acad. Sci. USA* **110**, 12229–12234 (2013).
17. Hutchison, S. G., Richardson, L. S. & Wai, C. M. Carbothermic reduction of silicon dioxide – a thermodynamic investigation. *Metall. Mater. Trans. B* **19**, 249–253 (1988).
18. Bok, T., Choi, S., Lee, J. & Park, S. Effective strategies for improving the electrochemical properties of highly porous Si foam anodes in lithium-ion batteries. *J. Mater. Chem. A* **2**, 14195–14200 (2014).
19. Ryu, J., Hong, D., Choi, S. & Park, S. Synthesis of ultrathin Si nanosheets from natural clays for lithium-ion battery anodes. *ACS Nano* **10**, 2843–2851 (2016).
20. Liu, X. F., Giordano, C. & Antonietti, M. A molten-salt route for synthesis of Si and Ge nanoparticles: chemical reduction of oxides by electrons solvated in salt melt. *J. Mater. Chem.* **22**, 5454–5459 (2012).
21. Lin, N. et al. A low temperature molten salt process for aluminothermic reduction of silicon oxides to crystalline Si for Li-ion batteries. *Energy Environ. Sci.* **8**, 3187–3191 (2015).
22. Zhou, Z. W., Liu, Y. T., Xie, X. M. & Ye, X. Y. Aluminothermic reduction enabled synthesis of silicon hollow microspheres from commercialized silica nanoparticles for superior lithium storage. *Chem. Commun.* **52**, 8401–8404 (2016).
23. Lin, N. et al. Preparation of nanocrystalline silicon from $SiCl_4$ at 200 °C in molten salt for high-performance anodes for lithium ion batteries. *Angew. Chem. Int. Ed.* **54**, 3822–3825 (2015).
24. Aarset, K., Shen, Q., Thomassen, H., Richardson, A. D. & Hedberg, K. Molecular structure of the aluminum halides, Al_2Cl_6, $AlCl_3$, Al_2Br_6, $AlBr_3$, and AlI_3, obtained by gas-phase electron-diffraction and ab initio molecular orbital calculations. *J. Phys. Chem. A* **103**, 1644–1652 (1999).
25. Yoshikawa, N., Kikuchi, A. & Taniguchi, S. Anomalous temperature dependence of the growth rate of the reaction layer between silica and molten aluminum. *J. Am. Ceram. Soc.* **85**, 1827–1834 (2002).
26. Li, X. L. et al. Mesoporous silicon sponge as an anti-pulverization structure for high-performance lithium-ion battery anodes. *Nat. Commun.* **5**, 4105 (2014).
27. Li, Y. Z. et al. Growth of conformal graphene cages on micrometre-sized silicon particles as stable battery anodes. *Nat. Energy* **1**, 15029 (2016).
28. Ryu, J., Hong, D., Shin, M. & Park, S. Multiscale hyperporous silicon flake anodes for high initial coulombic efficiency and cycle stability. *ACS Nano* **10**, 10589–10597 (2016).
29. Esmanski, A. & Ozin, G. A. silicon inverse-opal-based macroporous materials as negative electrodes for lithium ion batteries. *Adv. Funct. Mater.* **19**, 1999–2010 (2009).
30. Yen, Y. C., Chao, S. C., Wu, H. C. & Wu, N. L. Study on solid-electrolyte-interphase of Si and C-coated Si electrodes in lithium cells. *J. Electrochem. Soc.* **156**, A95–A102 (2009).
31. Delley, B. An all-electron numerical-method for solving the local density functional for polyatomic-molecules. *J. Chem. Phys.* **92**, 508–517 (1990).
32. Delley, B. From molecules to solids with the $DMol^3$ approach. *J. Chem. Phys.* **113**, 7756–7764 (2000).
33. Perdew, J. P., Burke, K. & Ernzerhof, M. Generalized gradient approximation made simple. *Phys. Rev. Lett.* **77**, 3865–3868 (1996).
34. Tkatchenko, A. & Xcheffler, M. Accurate molecular van der waals interactions from ground-State electron density and free-atom reference data. *Phys. Rev. Lett.* **102**, 073005 (2009).
35. Bell, S. & Crighton, J. S. Locating transition states. *J. Chem. Phys.* **80**, 2464–2475 (1984).
36. Halgren, T. A. & Lipscomb, W. N. The synchronous-transit method for determining reaction pathways and locating molecular transition states. *Chem. Phys. Lett.* **49**, 225–232 (1977).

Acknowledgements

This work was supported by the Future Technology Research Center, LG Chem. SKK acknowledges the financial support from UNIST (1.170012.01) and computational support from UNIST-HPC. CMW thanks the support of the Assistant Secretary for Energy Efficiency and Renewable Energy, Office of Vehicle Technologies of the U. S. Department of Energy under Contract No. DE-AC02-05CH11231, Subcontract No. 18769 and No. 6951379 under the Advanced Battery Materials Research (BMR) program.

The microscopic analysis in this work was conducted in the William R. Wiley Environmental Molecular Sciences Laboratory (EMSL), a national scientific user facility sponsored by DOE's Office of Biological and Environmental Research and located at PNNL. PNNL is operated by Battelle for the Department of Energy under Contract DE-AC05-76RLO1830.

Author contributions

G.S., J.R., and J.C.K. contributed equally to this work. S.P. conceived the concept. G.S., J.R., and S.K designed and carried out the experiments, physical characterization, and electrochemical test. G.S., J.R., and C.W. performed the ex situ and in situ TEM characterization and data analysis. J.C.K. and J.H.L. performed molecular modeling and simulation. G.S., J.R., J.C.K., J.H.L., S.K.K., and S.P. co-wrote the manuscript. All authors discussed the results and commented on the manuscript.

Additional information

Supplementary information accompanies this paper at https://doi.org/10.1038/s42004-018-0041-z.

Competing interests: The authors declare no competing interests.